# Ventilated metasurface absorber constructed by synthesized acoustic multipoles

Chen Liu,[1,§] Chun Gong,[2,3,§] Houyou Long,[1,*] Ye Gu,[1] Chengrong Ma,[1] Yimin Liu,[1] Yuanzhou Zhu,[1] Ying Cheng,[1,4,†] and Xiaojun Liu[1,4,‡]

[1] *Department of Physics, MOE Key Laboratory of Modern Acoustics, Collaborative Innovation Center of Advanced Microstructures, Nanjing University, Nanjing 210093, China*

[2] *School of Naval Architecture, Ocean and Civil Engineering, Shanghai Jiao Tong University, Shanghai 200240, China*

[3] *Media Corporate Research Center, Foshan 528300, China*

[4] *State Key Laboratory of Acoustics, Chinese Academy of Sciences, Institute of Acoustics, Beijing 100190, China*

(Received 1 December 2023; revised 22 March 2024; accepted 24 May 2024; published 18 June 2024)

Acoustic metasurfaces have paved the way for the ongoing development of compact sound-absorbing devices that possess excellent ventilation capabilities. However, existing absorption mechanisms primarily focus on plane-wave fronts while neglecting omnidirectionally radiated cylindrical waves. In this study, drawing inspiration from wave-interference theory, we propose an approach to absorb cylindrical sound waves by combining artificially decorated passive monopoles and dipoles, which are synthesized by a coiled space resonator and a double-channel resonator, respectively. To demonstrate the effectiveness of our approach, we construct an ultrasparse annular metasurface absorber with an air-channel-area ratio of 46% and a deep-subwavelength thickness. Remarkably, this absorber achieves an absorption performance of 96% (91% in the experiment) for omnidirectionally radiated cylindrical sound waves. This achievement is realized by utilizing a circular array composed of 36 metamolecules arranged in a ringlike grating structure, with each metamolecule supporting synthesized multipoles. The near-unity absorption is accomplished through destructive interference between the composite monopole and dipole, characterized using a one-dimensional impedance tube. This high-efficiency absorption, combined with excellent ventilation and compactness, introduces alternative possibilities for designing functional sound-absorbing devices that can handle low-frequency sound waves with complex wave fronts.

DOI: 10.1103/PhysRevApplied.21.064043

## I. INTRODUCTION

Manipulating highly efficient or even perfect wave absorption with low-profile devices has garnered significant interest in recent years across various branches of wave physics [1–3]. In acoustics, resonant mechanisms, such as spring-mass oscillation, quarter-wavelength resonance, and Mie resonance, have been proposed for the development of absorbing meta-atoms, including Helmholtz resonators [4–9], microperforated plates [10–12], Fabry-Perot resonators [13–16], membrane resonators [17–20], and Mie resonators [21–23]. These meta-atoms are capable of highly localizing sound energy during intense resonance, surpassing the limitations imposed by linear response theory, which governs conventional bulky porous materials. Thus, sound-absorbing devices based on metamaterials or metasurfaces exhibit superior performance, particularly in the consumption of low-frequency sound [3]. Additionally, the operating frequency can be tailored by adjusting the geometry of meta-atoms, and broadband absorbers can be achieved by coupling multiple meta-atoms with discrete resonant frequencies [14,15,24–30]. Furthermore, metasurfaces have been employed in the construction of absorbers in two-port open systems, showcasing not only highly efficient absorption but also air-ventilation and heat-dissipation capabilities [31–43]. However, most of these absorbers utilize a lossy meta-atom and an effective boundary connected in a cascading manner [31–34,36], which only considers the suppression of normally or obliquely impinged plane waves at specific angles and does not encompass omnidirectionally radiated cylinder sound. This restricts the potential applications of these absorbing devices.

In this study, a paradigm is proposed to realize an annulus metasurface absorber (AMA) that can absorb sound enclosed within a ringlike grating structure, based on the Jessel-Mangiante-Canevet (JMC) theory. The JMC theory is deduced from Huygens' principle and the Kirchhoff diffraction theory [44]. According to this theory,

*Corresponding author: longhouyou@nju.edu.cn
†Corresponding author: chengying@nju.edu.cn
‡Corresponding author: liuxiaojun@nju.edu.cn
§C. Liu and C. Gong contributed equally to this work.

 

by introducing continuously distributed secondary tripole (monopole and dipole) sources on the surface of the enclosure, the radiation of cylindrical sound can be suppressed through destructive interference. This concept is fundamental in the field of active noise control [45,46]. However, such processes cannot truly attenuate sound energy, not to mention the need for continuously providing additional electric energy.

In contrast, our study builds upon the JMC theory and presents an alternative approach for creating a ventilated AMA. This absorber combines discretely distributed passive monopoles and dipoles, which are of identical resonant frequency and generate out-of-phase reradiated sound. Consequently, both reflected and transmitted waves are effectively suppressed, leading to dissipation of sound energy within the resonant metamolecule framework. For the monopole component, we employ a coiled space resonator (CSR), while the dipole component is realized using a double-channel Mie resonator (DMR). To characterize these components in a one-dimensional system, we extract the effective acoustical parameters. By coupling the CSR and DMR, we achieve a metasurface absorber (MA) that demonstrates 98% absorption in simulations (95% in experiments) for a plane-sound wave at 724 Hz. We then utilize these MA metamolecules to construct an ultrasparse annulus metasurface absorber. Our AMA achieves 96% absorption in simulations (91% in experiments) for omnidirectionally radiated cylindrical sound, despite having an area ratio of the air channel as high as 46%. Additionally, our design leads to an approximately 15-dB reduction in sound-pressure level (SPL) compared to that observed in free space.

## II. MODEL OF ANNULUS METASURFACE ABSORBER

The JMC theory has demonstrated that the hybridization of monopole and dipole sources can result in zero backward reradiation. In our approach, instead of attempting the impractical task of continuously distributing active sources on the enclosed surface, we construct the AMA using discrete passive resonant monopoles and dipoles, as illustrated in Figs. 1(a) and 1(b). Figure 1(a) presents a three-dimensional (3D) stereogram of the proposed AMA, while Fig. 1(b) provides a two-dimensional (2D) top view. The inner radius ($R_1$) and outer radius ($R_2$) of the AMA are set at 0.47 and 0.53 m, respectively. To absorb sound emitted from the line source at its center, it is necessary to cancel out both reflected and transmitted waves, as depicted in Fig. 1(b). The wave equation in cylindrical coordinates, in the 2D scene, can be formulated as $\nabla^2 p = (1/r)(\partial/\partial r)\,(\rho(\partial p/\partial r)) + (1/r^2)(\partial^2 p/\partial\varphi^2)$. The general solution of this wave equation can be expressed as $p\,(r,\varphi) = \sum_n \sum_m \left[X_n H_n^{(1)}\,(k_0 r) + Y_n H_n^{(2)}\,(k_0 r)\right]\left(A_m \cos m\varphi + B_m \sin m\varphi\right)$. Here, the time harmonics have been

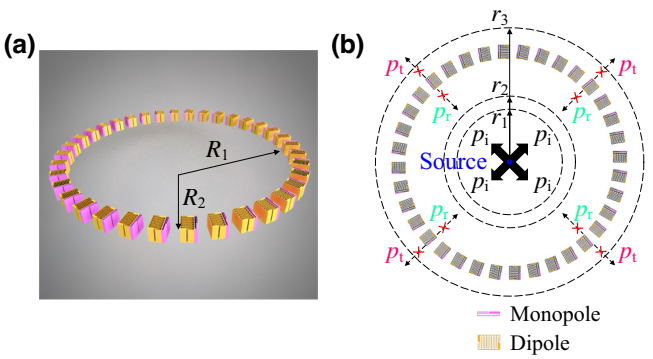


FIG. 1. (a) 3D stereogram and (b) 2D top view of the AMA with a line sound source placed at its center. $R_1$ and $R_2$ represent the physical inner and outer radii of the AMA structure, respectively. $r_1$, $r_2$, and $r_3$ denote the radii of artificially defined cylindrical surfaces for obtaining the scattering spectra of the AMA.

omitted. $H_0^{(1)}$ and $H_0^{(2)}$ represent the zero-order Hankel functions of the first kind (converging waves) and second kind (diverging waves), respectively. $k_0 = \omega/c_0$ represents the wave number, while $\omega$ denotes the angular frequency and $c_0$ denotes the sound velocity in air. Given the polar symmetry inherent in our scenario and the approximation of the AMA as a uniform layer, we set $m = 0$ and $n = 0$. To obtain the scattering spectra of the AMA, it is necessary to acquire sound pressure on three artificially defined cylindrical surfaces [circles denoted by dashed lines in Fig. 1(b)] with radii of $r_1$, $r_2$, and $r_3$ ($r_1 < r_2 < R_1$ and $r_3 > R_2$). Following the rigorous scattering theory, sound pressure within the AMA structure, encompassing both reflected and incident waves (characterized by the first and second types of Hankel functions), can be formulated as [47]

$$p_1 = X_1 H_0^{(1)}(k_0 r_1) + Y_1 H_0^{(2)}(k_0 r_1), \tag{1a}$$

$$p_2 = X_1 H_0^{(1)}(k_0 r_2) + Y_1 H_0^{(2)}(k_0 r_2), \tag{1b}$$

where the coefficients $X_1$ and $Y_1$ represent the backward and forward waves, respectively. On the other hand, sound pressure outside the AMA structure, due to the infinite external space, only considers the transmitted wave radiating outward, as expressed by

$$p_3 = Y_2 H_0^{(2)}(k_0 r_3). \tag{2}$$

Note that $p_1$, $p_2$, and $p_3$ denote sound pressure on cylindrical surfaces with radii $r_1$, $r_2$, and $r_3$, respectively, which can be retrieved through simulation.

By solving Eqs. (1) and (2), one can obtain the coefficients $X_1$, $Y_1$, and $Y_2$:

$$X_1 = \frac{H_0^{(2)}(k_0 r_2)p_1 - H_0^{(2)}(k_0 r_1)p_2}{H_0^{(1)}(k_0 r_1)H_0^{(2)}(k_0 r_2) - H_0^{(2)}(k_0 r_1)H_0^{(1)}(k_0 r_2)}, \quad (3a)$$

$$Y_1 = \frac{H_0^{(1)}(k_0 r_1)p_2 - H_0^{(1)}(k_0 r_2)p_1}{H_0^{(1)}(k_0 r_1)H_0^{(2)}(k_0 r_2) - H_0^{(2)}(k_0 r_1)H_0^{(1)}(k_0 r_2)}, \quad (3b)$$

$$Y_2 = \frac{p_3}{H_0^{(2)}(k_0 r_3)}. \quad (3c)$$

Thus, the reflection and transmission coefficients of sound pressure can be determined:

$$r_p = \frac{X_1}{Y_1} = \frac{p_1 H_0^{(2)}(k_0 r_2) - p_2 H_0^{(2)}(k_0 r_1)}{p_2 H_0^{(1)}(k_0 r_1) - p_1 H_0^{(1)}(k_0 r_2)},$$

$$t_p = \frac{Y_2}{Y_1} = \frac{p_3\left[H_0^{(1)}(k_0 r_1)H_0^{(2)}(k_0 r_2) - H_0^{(2)}(k_0 r_1)H_0^{(1)}(k_0 r_2)\right]}{H_0^{(2)}(k_0 r_3)\left[p_2 H_0^{(1)}(k_0 r_1) - p_1 H_0^{(1)}(k_0 r_2)\right]}. \quad (4)$$

The variables $p_1$, $p_2$, and $p_3$ represent sound pressure on cylindrical surfaces with respective radii of $r_1$, $r_2$, and $r_3$. By retrieving and substituting $p_1$, $p_2$, and $p_3$ into Eq. (4), we can derive the reflectance ($R = |r_p|^2$), transmittance ($T = |t_p|^2$), and absorptance ($A = 1 - R - T$) of sound energy (see Appendix A for a detailed deduction).

## III. RESULTS AND DISCUSSION

### A. MA for dissipating plane wave

To explore the absorption mechanism of the AMA, we first analyze the acoustical performances of the composed meta-atoms in Figs. 2(a) and 2(b), as well as the synthesized metamolecule in Fig. 2(c), within a one-dimensional MA setting. The relevant geometrical features are indicated in the figures. Specifically, $W_1$ and $W_2$ denote the outer widths in the $y$ direction of the CSR and DMR, respectively. Correspondingly, $w_1$ and $w_2$ represent the respective channel widths, while $t$ represents the thickness of the walls. Therefore, we can compute $l_1 = (L - w_1)/2$ and $l_2 = (W_2 - w_2)/2$. Notably, the reflected sound waves generated by monopolar CSR meta-atoms (dipolar DMR meta-atoms) exhibit an antiphase (in-phase) relationship with the incident sound wave, as shown in Fig. 2(a) [Fig. 2(b)]. Consequently, the interaction of the reflected sound

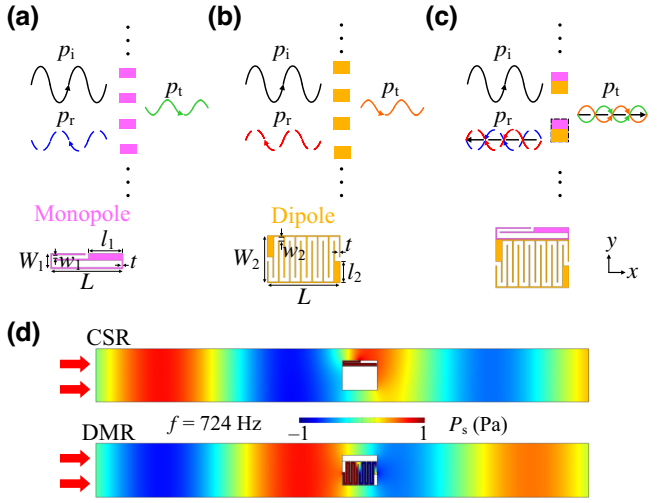


FIG. 2. Schematic diagrams of the metasurface comprising (a) monopolar meta-atoms, (b) dipolar meta-atoms, and (c) synthesized multipolar metamolecules, arranged in a sparsely populated array with ventilation channels. Insets, 2D cross sections of the physical structures for each corresponding element. (d) Scattered sound fields corresponding to CSR and DMR meta-atoms at 724 Hz.

waves from the synthesized multipolar metamolecules produces destructive interference, leading to minimal reflection. This effect is similarly observed with transmitted waves due to the mirror symmetry of monopoles and antimirror symmetry of dipoles, as illustrated in Fig. 2(c). Additionally, we present the scattered sound fields of CSR (upper panel) and DMR (lower panel) in Fig. 2(d). It is observed that the reflected and transmitted sound waves for CSR and DMR are approximately 180° out of phase with each other, which is consistent with the theoretical analysis. Consequently, the bidirectional quasiperfect absorption arises from the combination of low reflection and transmission.

As a demonstration, we have designed a MA device operating at 724 Hz. Figures 3(a) and 3(b) present the simulated reflectance (black dashed curve), transmittance (blue dashed-dotted curve), and absorptance (red solid curve) of standalone CSR and DMR meta-atoms, respectively. Notably, losses in the metasurfaces originate from thermal viscous dissipation due to friction between air particles and the solid framework. To characterize this dissipation effect, complex constitutive parameters, including mass density and the bulk modulus with imaginary parts representing thermal viscous losses, are incorporated following the Stinson model [48]. In the simulation, we initially determine the values of effective mass density and bulk modulus at specific frequencies, which are then expressed as an interpolated function of frequency in COMSOL Multiphysics. Consequently, channels with varying widths at different frequencies can be adequately

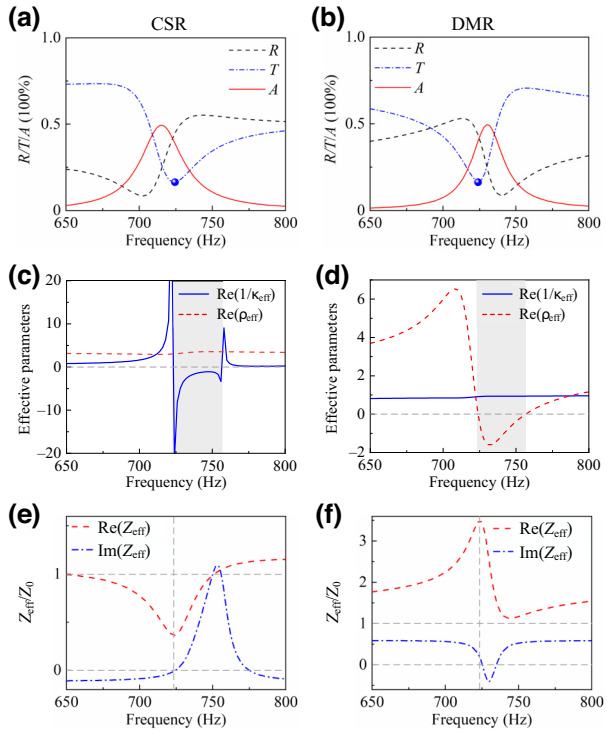


FIG. 3. Simulated acoustic spectra: reflectance $R$, transmittance $T$, and absorptance $A$ of (a) the CSR and (b) DMR. (c),(d) Corresponding real part of the normalized effective mass density and compression modulus. (e),(f) Normalized effective impedances.

accounted for. The waveguide has a width of 0.09 m, and the other geometrical parameters are listed in Table I. It is observed that both CSR and DMR exhibit transmission dips at 724 Hz, indicating the occurrence of resonances. However, the resonant mechanisms differ between CSR and DMR. To clarify this, we retrieved the real part of the normalized effective mass density, $\rho_{\text{eff}}$, and compression modulus, $1/\kappa_{\text{eff}}$, of CSR and DMR [49], as shown in Figs. 3(c) and 3(d), respectively. The results reveal that CSR and DMR exhibit negative $1/\kappa_{\text{eff}}$ and $\rho_{\text{eff}}$ at resonance, suggesting monopole and dipole resonant modes, respectively. To gain a deeper insight, we also investigate the sound impedance, $Z_{\text{eff}}$, of CSR and DMR, which are almost purely real at 724 Hz, with values of $0.364 - 0.0042j$ and $3.496 + 0.032j$, respectively, as shown in Figs. 3(e) and 3(f). Thus, CSR behaves acoustically as a soft boundary, while DMR behaves as a hard wall.

TABLE I. Geometric parameters of CSR and DMR (units, mm).

| $W_1$ | $W_2$ | $w_1$ | $w_2$ | $t$ | $L$ |
|---|---|---|---|---|---|
| 10.1 | 40.3 | 2.4 | 3.6 | 1 | 60.8 |

We proceed to characterize the acoustical performance of the assembled absorptive system, as depicted in Fig. 2(c). Figure 4(a) presents the acoustic spectra of the MA device, where lines and symbols correspond to the numerical and experimental results, respectively. We conducted the experimental measurements using the standard ASTM E2611-09 [50], employing an impedance tube made of Plexiglass (see Appendix C). The absorber specimen was manufactured using 3D-printing technology with epoxy resin [with a mass density of $\rho_e = 1050$ kg/m$^3$ and a sound velocity of $c_e = 2200$ m/s; see inset in Fig. 4(b)]. It is observed that both the reflectance and transmittance of the MA device at 724 Hz are near zero, resulting in quasiperfect absorption (98% in the simulation and 95% in the experiment). Here, the necessity of dipole and monopole characteristics for near-perfect absorption is discussed (see Appendix D). The scattering phenomena of monopoles and dipoles can be decomposed into symmetric and antisymmetric reflection problems [38]. Consequently, achieving perfect absorption entails the degenerate monopoles and dipoles in a critical coupled state displaying maximum absorption of 0.5 under one-sided illumination, consistent with conditions derived from coupled-mode theory [51]. The surface impedance of the MA device was calculated, as shown in Fig. 4(b). The results demonstrate that the surface impedance at 724 Hz, obtained from finite-element method simulations (experimental measurements), is $1.005 - 0.009j$ ($1.011 - 0.044j$), which excellently matches the impedance of the air medium. The differences between the experimental and numerical results may arise from the constrained thickness (10 mm) of the impedance tube preventing the simulation of a rigid boundary; the restricted manufacturing precision (1 mm) of the specimens; and the finite length (0.8 m) of the absorbing materials, which hinders the replication of a perfectly matched layer utilized in numerical simulations. Additionally, while our primary focus has been on airborne sound applications, this concept also offers the potential for the implementation of absorption in a broader range of systems and frequencies, including those in underwater environments (see Appendix E).

To visually demonstrate the acoustic characteristics, we present the distribution of the absolute sound pressure at 724 Hz in Fig. 4(c) (upper panel). In the simulation, a plane sound wave radiates from the left port. It can be observed that the sound energy is highly concentrated in the composite CSR and DMR element. Furthermore, it is evident that the CSR excites a monopolar resonance, while the DMR induces a dipolar resonance. Due to intense resonances, a significant amount of sound energy is dissipated within the composite resonators, as shown by the power-dissipation density given by $Q_{\text{PW}} = -2|\mathbf{I}|\text{Im}(k)$, where $|\mathbf{I}|$ denotes sound intensity and $k$ is the wave number [middle panel of Fig. 4(c)]. Consequently, the MA device exhibits a low reflectance and low transmittance, which is confirmed by

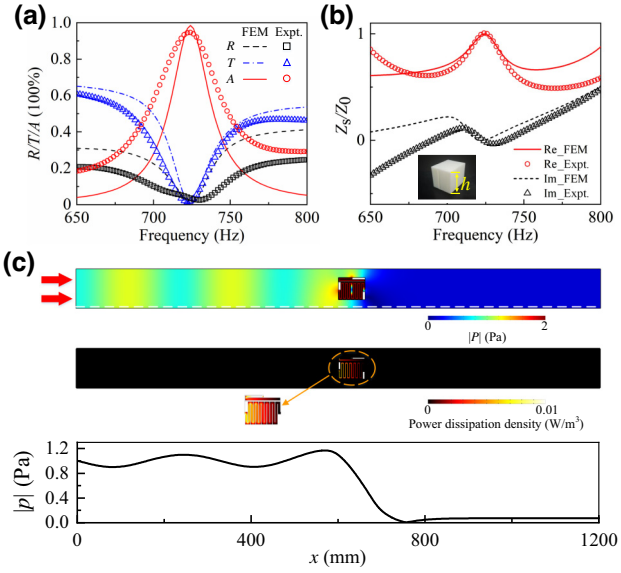


FIG. 4. (a) Acoustical scattering spectra and (b) normalized surface impedances of the MA. Lines and symbols represent numerical and experimental results, respectively. (c) Distribution of the absolute sound pressure (top panel), power dissipation density (middle panel), and profile of absolute sound pressure along the white dashed line (bottom panel) at 724 Hz.

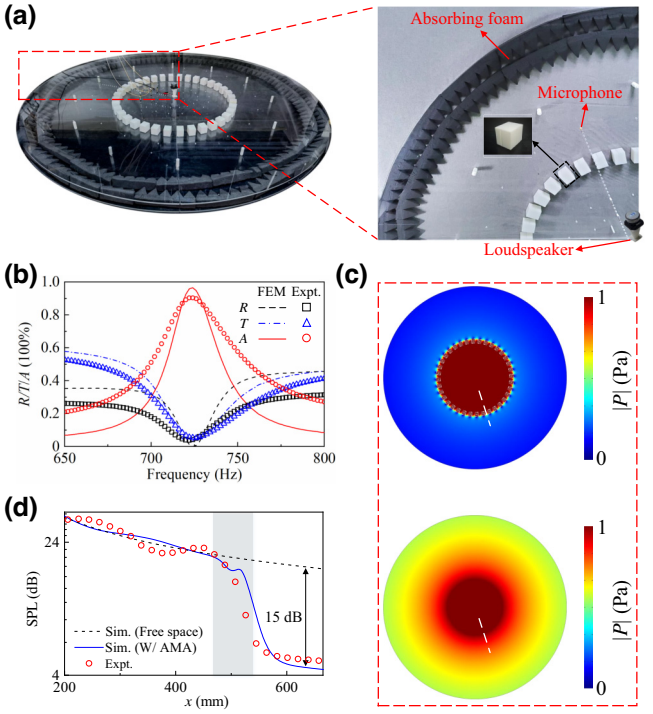


FIG. 5. (a) Experimental setup of the AMA composed of 36 MA metamolecules. (b) Scattering spectra of the AMA. Lines and symbols represent numerical and experimental results, respectively. (c) Distributions of the absolute sound pressure in systems with (upper panel) and without the AMA (lower panel). (d) Simulated (solid line) and measured (symbols) SPL along a radial axis. Dashed line represents the SPL distribution in free space for comparison.

the distribution of absolute sound pressure along the bottom line of the waveguide [lower panel of Fig. 4(c)]. The upstream region demonstrates a near-unity amplitude distribution of sound pressure, while the downstream region shows a near-zero amplitude distribution. Thus, the MA device achieves quasiperfect absorption for plane waves.

### B. Annulus metamaterial absorber

It is elucidated that radiation suppression can be achieved through the coupling of active monopoles and dipoles, a theory that has been utilized in the construction of an active annulus sound absorber [44]. Based on the proposed methodology, we have developed a passive AMA by arranging 36 predetermined metamolecules in a ringlike grating pattern, as depicted in Fig. 1. Each metamolecule occupies a sector of 10° in the azimuthal direction, with an air channel of 4.6° between adjacent metamolecules. Consequently, the area ratio of the air channel is 46%. To measure the acoustic spectra of the AMA, we configured an experimental setup as shown in Fig. 5(a). The AMA specimens were placed inside a waveguide formed by two parallel circular plates (with a thickness of 0.01 m and a diameter of 2.4 m) made of acrylic materials. A loudspeaker connected to a 3D-printed horn-shaped pipe was used to simulate a cylindrical sound source, and cone-shaped sound-porous materials were placed at the waveguide's end to simulate an anechoic boundary. Sound pressures were measured at three radial positions (0.2, 0.3, and 0.7 m) to obtain the acoustic scattering spectra. To reduce experimental error, sound pressure was recorded at intervals of $\pi/9$ in the azimuthal direction and averaged. Scattering coefficients were then calculated by substituting the retrieved sound pressures into Eq. (4).

Figure 5(b) presents the acoustical spectra of the AMA, with the simulated and measured results shown as lines and open symbols, respectively. The simulation (experiment) reveals near-zero reflectance and transmittance at 724 Hz (722 Hz), resulting in highly efficient absorption of 96% (91%). For better visualization, Fig. 5(c) illustrates the absolute sound-pressure distribution both with (upper panel) and without (lower panel) the AMA. The figures clearly show that the AMA blocks sound pressure, indicating negligible transmission, while the sound pressure inside the AMA remains similar to the sound pressure in free space without the AMA, implying minimal reflection. To further quantify this, Fig. 5(d) displays the profiles of sound-pressure level (SPL) along the radius [the white dashed line in Fig. 5(c)]. The results demonstrate that the SPL at 724 Hz significantly attenuates when passing through the AMA, resulting in a decrease of approximately 15 dB compared to free space.

Additionally, the similarity between SPL with and without the AMA in the region $r < R_1$ suggests minimal reflection of sound. Furthermore, a 3D meta-absorber, utilizing MAs on all six faces, has been constructed (see Appendix F). Research findings indicate that sound-insulation levels of 16 and 12 dB can be achieved along directions normal and parallel to the line source, respectively. It is worth noting that the efficient ventilated sound-absorbing performance mentioned above is achieved by an AMA with a thickness of $R_2 - R_1 = 0.06$ m, which corresponds to the subwavelength scale. In our experiments, we have incorporated 10-mm-thick acrylic plates to minimize pressure leakage and ensure adequate sound isolation. Additionally, we have added 1-mm-deep grooves, shaped similarly to AMA metamolecules, on the upper and lower acrylic plates. This design facilitates the seamless embedding of sandwiched AMA samples, reducing joints between the acrylic boards and the AMA structures along the transmission waveguides. Despite these measures, some level of leakage is inevitable and may impact the measured results. For instance, the leaked sound energy, especially at nonresonant frequencies, can be mistakenly perceived as additional absorption, leading to broadened absorption peaks in the measured results.

Finally, we conducted an investigation into the absorption characteristics of the AMA with varying inner radii $R_1$. Figure 6(a) illustrates the absorptance at 724 Hz, where $R_1$ ranges from 0.32 to 0.62 m in increments of 0.03 m (filling ratios of the ventilated channel are 16%, 23%, 29%, 34%, 40%, 46%, 52%, 58%, 64%, 70%, and 76%). It is noteworthy that the absorptance reaches its peak at $R_1 =$ 0.47 m and remains consistently high across the observed range of $R_1$, with over 82% absorption achieved. Moreover, the absorptance of the AMA is also investigated with different numbers of MA metamolecules, as shown in Fig. 6(b). The results indicate that the absorptance varies from 21% to 96% as the number of metamolecules increases from 3 to 46; it tends to stabilize once the number surpasses 36. Importantly, the absorptance exhibits robustness to changes in the number of metamolecules, as an AMA composed of 24 metamolecules still achieves an absorptance of over 80%. Note that variations in the ring radius or the number of metamolecules lead to changes in the filling ratio of the ventilated channel, significantly impacting the coupling intensity between the CSR and DMR. Near-unity absorptive peaks are achieved when nearly critical coupling conditions are met. Additionally, we examined the scattering coefficients of four absorbers with nearly identical filling ratios of the ventilated channel (see Appendix G). It is observed that, with similar filling ratios of the ventilated channel, the absorptive peak increases with the ring radius because the incident cylindrical wave tends to behave more like a plane wave in an AMA with a larger $R_1$. Therefore, the absorption peak of an AMA with a larger $R_1$ is closer to that of the MA. Furthermore, it is confirmed that the operating frequency is minimally affected by the ring radius and the number of molecules.

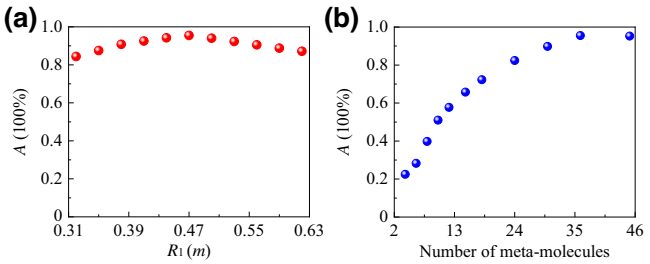


FIG. 6. Absorptance of the AMA at 724 Hz with variations in (a) inner radius $R_1$ and (b) number of metamolecules.

## IV. CONCLUSION

This work presents an approach for dissipating omnidirectionally radiated sound through the coupling of discretely distributed passive monopoles and dipoles, resulting in out-of-phase reflections and transmissions. To demonstrate the feasibility of this approach, we constructed an ultrasparse AMA with an air-channel-area ratio of 46%. By circularly arraying metamolecules consisting of a CSR and DMR, the AMA achieves near-unity absorption, with simulation and experimental results showing absorption rates of 96% and 91%, respectively, for cylindrical sound. This near-unity absorption is a result of destructive interference between the passive monopole and dipole components. The high-efficiency absorption and exceptional ventilation characteristics of the AMA render it a promising solution for various applications that demand low-frequency sound cancellation in subwavelength thicknesses.

## ACKNOWLEDGMENTS

This work was supported by the National Key R&D Program of China (2022YFA1404400), NSFC (Grants No. 12225408, No. 11834008, No. 12074183, No. 12004176, and No. 12374438).

## APPENDIX A: 2D CYLINDRICAL WAVE SOUND-ABSORPTION THEORY

To calculate the scattering spectra for sound energy, it is necessary to characterize the sound intensity. According to the relationship $v = -(1/j\omega\rho_0)\nabla p$, the particle velocities for the incident, reflected (at $R_1$), and transmitted (at $R_2$) sound waves can be expressed as

$$v_i = -\frac{Y_1}{jZ_0}\left[H_0^{'(2)}(k_0R_1)\right], \tag{A1a}$$

$$v_r = -\frac{X_1}{jZ_0}\left[H_0^{'(1)}(k_0R_1)\right], \tag{A1b}$$

$$v_t = -\frac{Y_2}{jZ_0}\left[H_0^{'(2)}(k_0R_2)\right]. \tag{A1c}$$

By substituting Eqs. (4) and (A1) into the equation $I = \frac{1}{2}\mathrm{Re}\{pv^*\}$, we can derive the sound intensities for the incident, reflected, and transmitted waves:

$$I_i = \frac{Y_1^2}{2Z_0}\left\{J_0(k_0R_1)N_0^{'}(k_0R_1) - N_0(k_0R_1)J_0^{'}(k_0R_1)\right\}, \tag{A2a}$$

$$I_r = \frac{X_1^2}{2Z_0}\left\{N_0(k_0R_1)J_0^{'}(k_0R_1) - J_0(k_0R_1)N_0^{'}(k_0R_1)\right\}, \tag{A2b}$$

$$I_t = \frac{Y_2^2}{2Z_0}\left\{J_0(k_0R_2)N_0^{'}(k_0R_2) - N_0(k_0R_2)J_0^{'}(k_0R_2)\right\}, \tag{A2c}$$

where $J_0(k_0r)$ and $N_0(k_0r)$ are the zero-order Bessel and Neumann functions, respectively, which satisfy the relationships $H_0^{(1)}(k_0r) = J_0(k_0r) + jN_0(k_0r)$ and $H_0^{(2)}(k_0r) = J_0(k_0r) - jN_0(k_0r)$. The scattering coefficients for sound energy can be obtained through some algebraic manipulation, given by

$$R = \frac{I_rS_1}{I_iS_1} = \left|\frac{X_1^2}{Y_1^2}\right| = |r_p|^2, \tag{A3a}$$

$$T = \frac{I_tS_2}{I_iS_1} = \left|\frac{Y_2^2}{Y_1^2}\right| = |t_p|^2. \tag{A3b}$$

The absorption coefficient is obtained by $A = 1 - R - T$.

In experiments, three radial positions ($p_1$, $p_2$, and $p_3$) are selected for data acquisition. To minimize experimental error, sound pressure is measured at various azimuthal positions and averaged. By substituting the recorded sound pressures into Eqs. (1)–(A3), experimental spectra can be obtained. These spectra are represented by the open symbols in Fig. 5(b).

## APPENDIX B: EFFECT OF VISCOTHERMAL LOSS

To analyze the viscothermal effects on sound-wave propagation in a narrow channel, we introduce the concept of complex effective mass density and bulk modulus using the Stinson model [48]. The effective mass density, $\rho_{\mathrm{eff}}$, and compressibility, $C_{\mathrm{eff}}$, are defined as

$$\rho_{\mathrm{eff}} = \rho_0\frac{\nu a^2b^2}{64j\omega}\left\{\sum_{m=0}^{\infty}\sum_{n=0}^{\infty}\left[\alpha_m^2\beta_n^2(\alpha_m^2+\beta_n^2+\frac{j\omega}{\nu})\right]^{-1}\right\}^{-1}, \tag{B1}$$

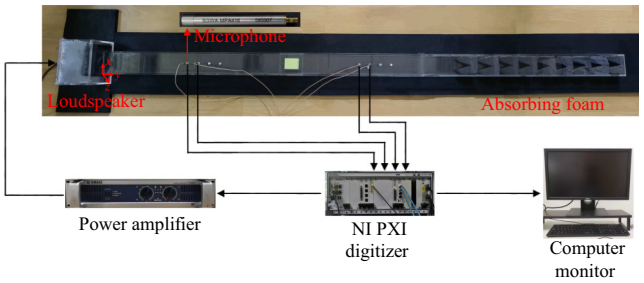


FIG. 7. Photograph of the experimental measurement setup.

$$C_{\mathrm{eff}} = \frac{1}{P_0}\left\{1 - \frac{64j\omega(\gamma-1)}{\nu' a^2b^2}\sum_{m=0}^{\infty}\sum_{n=0}^{\infty}\left[\alpha_m^2\beta_n^2(\alpha_m^2+\beta_n^2 + \frac{j\gamma\omega}{\nu'})\right]^{-1}\right\}. \tag{B2}$$

In these equations, we define the constants $\alpha_m = (2m+1)\pi/a^2$ and $\beta_n = (2n+1)\pi/b^2$, where $a$ and $b$ represent the side widths of a rectangular channel. The variables $\nu = \mu/\rho_0$ and $\nu' = \kappa/\rho_0C_v$ are defined with respect to air properties, specifically the air density ($\rho_0 = 1.21\ \mathrm{kg/m^3}$), dynamic viscosity ($\mu = 1.814\times10^{-5}$ Pa s), thermal conductivity ($\kappa = 2.624\times10^{-2}$ W/(m K)), heat capacity [$C_v = 0.7178\times10^3$ kJ/(kg K)], standard atmosphere pressure ($P_0 = 1.013\times10^5$ Pa), and the specific heat ratio of air ($\gamma = 1.4$). Thus, the effective wave number and impedance can be calculated as $k_{\mathrm{eff}} = \omega\sqrt{\rho_{\mathrm{eff}}/\kappa_{\mathrm{eff}}}$ and $z_{\mathrm{eff}} = \sqrt{\kappa_{\mathrm{eff}}\rho_{\mathrm{eff}}}$.

## APPENDIX C: EXPERIMENTAL SETUP

In this study, the experimental measurement of the MA is conducted using the standard ASTM E2611-09 [50]. The experimental setup is depicted in Fig. 7. The waveguide has side widths of $l_z = 0.05$ m and $l_x = 0.09$ m, with a wall thickness of 0.01 m. Thus, the cutoff frequency is determined to be 1905.6 Hz. The metasurface sample is fabricated using 3D-printing technology and is positioned in the middle of the impedance tube. To achieve anechoic conditions, a cone-shaped sound-absorbing foam with a length of 0.8 m ($> \lambda/4$) acts as the anechoic load.

During the measurement, input signals are generated by a waveform generator (NI PXI-5421) and amplified using an audio power amplifier (YAMAHA P2500S). A loudspeaker (Peerless TC6WD01-04) is positioned on the input surface of the tube to generate incident plane waves, while four 1/4-inch condenser microphones (GRAS 40 PH) are inserted into the waveguide to capture sound information. Data collected by the signal-acquisition board (NI PXI-4498), controlled by the LabVIEW program, are processed using the MATLAB package.

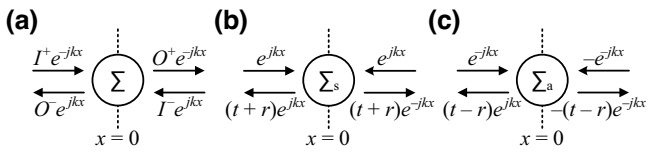


FIG. 8. (a) Schematic of an absorber with mirror symmetry. (b),(c) Schematics of symmetric and antisymmetric reflections, respectively.

## APPENDIX D: THEORETICAL ANALYSIS

The numerical and experimental results have demonstrated quasiperfect absorption. To demonstrate the essential roles of dipole and monopole characteristics in achieving near-perfect sound absorption, we analyze a general absorber with mirror symmetry, as depicted in Fig. 8(a). The scattering behavior of the absorber can be represented as

$$\begin{bmatrix} O^+ \\ O^- \end{bmatrix} = \mathbf{S} \begin{bmatrix} I^+ \\ I^- \end{bmatrix} = \begin{bmatrix} t & r \\ r & t \end{bmatrix} \begin{bmatrix} I^+ \\ I^- \end{bmatrix}, \tag{D1}$$

where $r$ and $t$ denote the reflection and transmission coefficients of sound pressure, respectively. For single-sided incidence, the absorption is defined as $A = 1 - |r|^2 - |t|^2$. Therefore, perfect absorption necessitates $r = t = 0$. Furthermore, the scattering analysis of an arbitrary structure with mirror symmetry can be separated into two reflection subproblems [38,52]. Specifically, a symmetric and an antisymmetric reflection scenario, where the reflected coefficients corresponding to the eigenvalues of the scattering matrix are formulated as $\lambda_\pm = t \pm r$, as illustrated in Fig. 8(b) and 8(c).

Initially, we examine a symmetric scatter. The scattering relationship (omitting the $e^{-jkx}$ and $e^{jkx}$ terms) can be written as

$$\begin{bmatrix} r+t \\ r+t \end{bmatrix} = \begin{bmatrix} t_s & r_s \\ r_s & t_s \end{bmatrix} \begin{bmatrix} 1 \\ 1 \end{bmatrix}. \tag{D2}$$

For an antisymmetric scatter, the relationship is expressed as

$$\begin{bmatrix} r-t \\ t-r \end{bmatrix} = \begin{bmatrix} t_a & r_a \\ r_a & t_a \end{bmatrix} \begin{bmatrix} 1 \\ -1 \end{bmatrix}. \tag{D3}$$

Therefore, we can derive the following expressions:

$$r = [(t_s + r_s) + (t_a - r_a)]/2, \tag{D4}$$

$$t = [(t_s + r_s) - (t_a - r_a)]/2. \tag{D5}$$

Here, $t_s$ and $r_s$ ($t_a$ and $r_a$) represent the transmission and reflection coefficients of symmetric (antisymmetric) scatters. Notably, a monopole (dipole) exhibits symmetric (antisymmetric) sound-pressure distributions. Hence, treating the reflection subproblems of symmetric and antisymmetric scatters as scattering problems of monopoles and dipoles, respectively, leads to the construction of a mirror-symmetric sound absorber. It is noteworthy that sound-pressure continuity is maintained for a monopole, specifically at the opening of the folded Fabry-Perot (FP) resonator utilized in this study, resulting in $1 + r_s = t_s$. On the contrary, for an ideal dipole, such as a decorated membrane resonator, particle-velocity continuity is demonstrated, resulting in $1 - r_a = t_a$. Thus, we simplify Eqs. (D4) and (D5) as

$$r = 1 + (r_s - r_a), \tag{D6}$$

$$t = r_s + r_a. \tag{D7}$$

Perfect absorption can be achieved when $r_s = -0.5$, $t_s = 0.5$, and $r_a = t_a = 0.5$ are attained at the same frequency, indicating the degeneration of monopolar and dipolar resonances. In cases where only a monopole or dipole is excited, the absorption is calculated as $A_s = 1 - |r_s|^2 - |t_s|^2 = 0.5$ and $A_a = 1 - |r_a|^2 - |t_a|^2 = 0.5$, representing the maximal absorption value for an ideal monopole and dipole, respectively. In summary, achieving perfect absorption necessitates the presence of degenerate monopoles and dipoles in a critically coupled state, demonstrating a maximum absorption of 0.5 under one-side illumination, in alignment with the conditions derived from coupled-mode theory [51].

For verification, we have reconfigured an absorber with the geometric specifications detailed in Table II; this achieves perfect absorption at 724 Hz, as shown in Fig. 9. Here, both the monopole and dipole exhibit resonance at 724 Hz, with absorption rates of 49.7% and 49.9%, respectively. Nevertheless, the practical constraints of 3D printing, with a precision limit of 1 mm, prevent the fabrication of the absorber with the precise geometric dimensions. As a result, we devise a MA device in the manuscript to achieve near-perfect absorption for incident plane waves.

TABLE II. Geometric parameters of CSR and DMR (units, mm).

| $W_1$ | $W_2$ | $w_1$ | $w_2$ | $t$ | $L$ |
|---|---|---|---|---|---|
| 9.8 | 40.3 | 2.26 | 3.56 | 1 | 60.28 |

## APPENDIX E: MA SYSTEM FOR UNDERWATER SOUND

The absorptive mechanism proposed in the MS could have universal applicability across different fluid background media and various frequency ranges. To illustrate

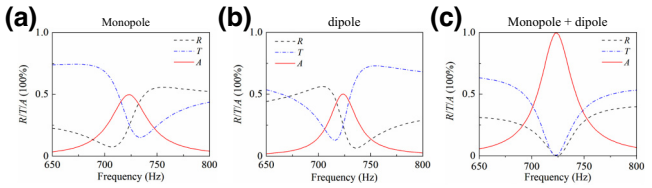


FIG. 9. Acoustic spectra of (a) monopole only, (b) dipole only, and (c) a combination of monopole and dipole.

this concept, we present a numerical demonstration of an underwater sound absorber, as depicted in Fig. 10. The simulation is carried out using the acoustic–solid-interaction frequency-domain module in COMSOL Multiphysics, accounting for the fluid-structure coupling effect of thin solid plates in a water environment. The CSR and DMR materials are modeled as steel with a mass density of 7850 kg/m$^3$, Young's modulus of 205 GPa, and Poisson's ratio of 0.28. The simulation is conducted under atmospheric pressure at a temperature of 20 °C. The relevant geometric parameters are detailed in Table III. Key material properties and fluid parameters such as dynamic viscosity ($\mu = 1.01 \times 10^{-3}$ Pa s), thermal conductivity [$\kappa = 0.6$ W/(m K)], heat capacity [$C_v = 4.18 \times 10^3$ kJ/(kg K)], and the specific heat ratio of water ($\gamma = 1.01$) are employed to characterize the viscous and thermal dissipation [53].

The scattering spectra of the designed underwater MA are illustrated in Fig. 10(a), demonstrating 99.8% absorption at 3.18 kHz with a subwavelength size smaller than 1/10 of the operating wavelength. Figure 10(b) further exhibits the corresponding absolute sound-pressure distribution for enhanced visualization of these acoustic characteristics, highlighting the concentration and dissipation of sound energy primarily by the CSR and DMR components.

Additionally, it is worth mentioning that the configuration of the open resonant cavity in synthesized multipolar metamolecules, which are connected to the external environment, allows it to operate under high-water-pressure conditions. The main challenge arises from the elastic vibration of the solid frames induced by the fluid-structure coupling effect, as illustrated in Figs. 10(c) and 10(d), particularly under high-intensity incidence. This issue could be addressed by incorporating reinforcing ribs to enhance the structure's stiffness, thus reducing distortion and alleviating stress concentration.

TABLE III. Geometric parameters of CSR and DMR (units, mm).

| $W_1$ | $W_2$ | $w_1$ | $w_2$ | $t$ | $L$ |
|---|---|---|---|---|---|
| 6.74 | 26.7 | 1.32 | 2.2 | 1 | 42.6 |

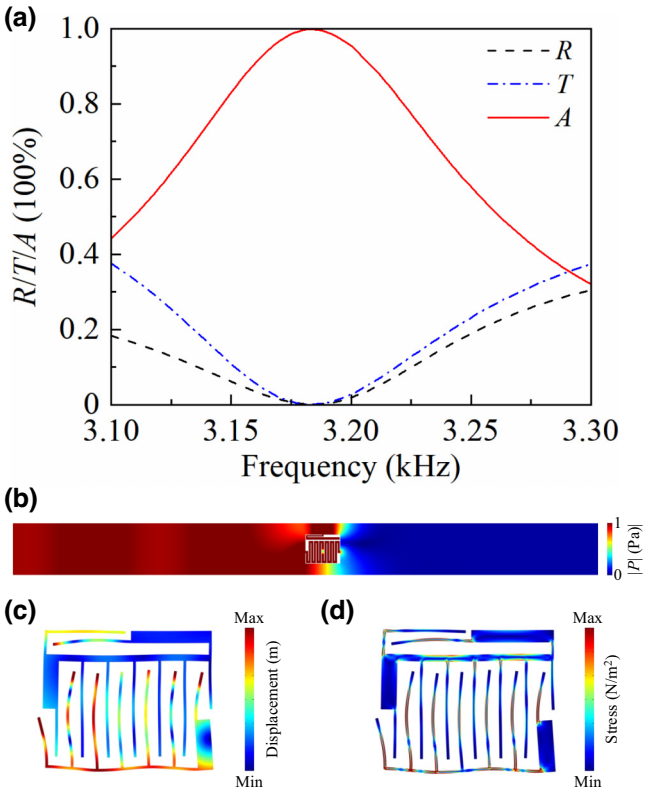


FIG. 10. (a) Acoustic scattering spectra of an underwater absorptive system. (b) Distribution of the absolute sound pressure at 3.18 kHz. (c),(d) Corresponding displacement and stress distribution, respectively, in the solid frames of the multipolar metamolecules.

## APPENDIX F: THREE-DIMENSIONAL META-ABSORBER

In addition to the 2D AMA in the MS, we have developed a 3D cubic meta-absorber in which all six faces utilize MAs, as depicted in Fig. 11(a). Assuming the cylindrical line sound source along the $z$ direction as the noise source to be eliminated, this 3D meta-absorber consists of five MAs parallel to the line source and three MAs normal to the line source on each face. The remaining parameters are consistent with the MA structure presented in Fig. 2 of the main text. In Fig. 11(b), the simulated sound-field distribution is displayed, demonstrating a concentration of sound energy within the absorber. Figures 11(c) and 11(d) showcase the SPL profiles along the red dashed lines depicted in Fig. 11(b). The results indicate that sound-insulation levels of 16 and 12 dB are achieved in directions normal and parallel to the line source, respectively.

Similarly, we can also design a 3D spherical meta-absorber with multipolar metamolecules evenly distributed in the shell, as illustrated in Fig. 12(a). The outcomes in Figs. 12(c)–12(d) distinctly demonstrate the effective

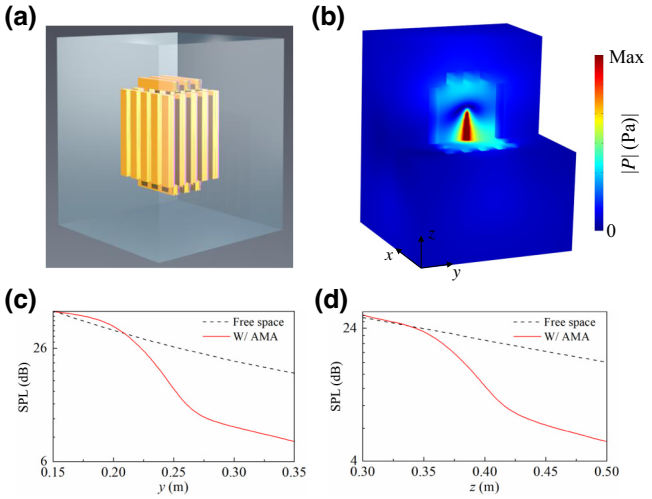


FIG. 11. (a) Sketch of numerical experimental setup. (b) Absolute sound-pressure distribution at 724 Hz. (c),(d) Profiles of SPLs along the red dashed lines shown in (b).

absorption of spherical wave radiation from a point source located at the center.

## APPENDIX G: INFLUENCE OF VENTILATION AREA

To investigate the relationship between the absorption characteristics and the ventilation area, we conducted a detailed analysis of the scattering spectra for four scenarios with approximately the same ratios of the ventilated channel area (46%, for example), as depicted in Figs. 13(a)–13(d). In these cases, the number of AMA molecules

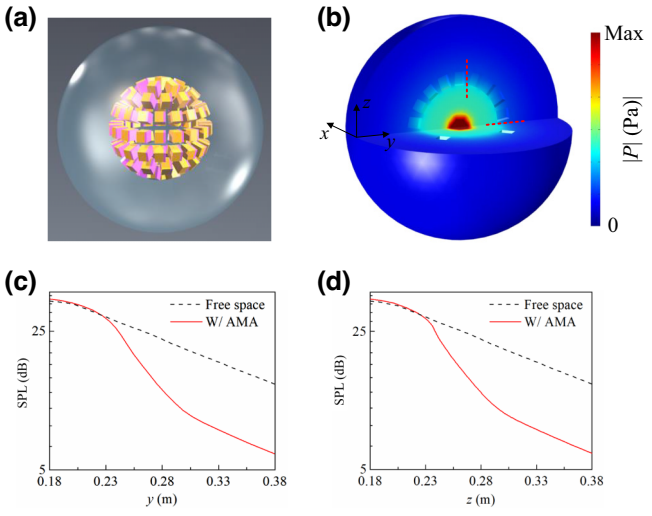


FIG. 12. (a) Sketch of a spherical sample in the numerical simulations. (b) Cross-section view of the absolute sound-pressure distribution at 724 Hz. (c),(d) SPL profiles along the horizontal and vertical red dashed lines indicated in (b).

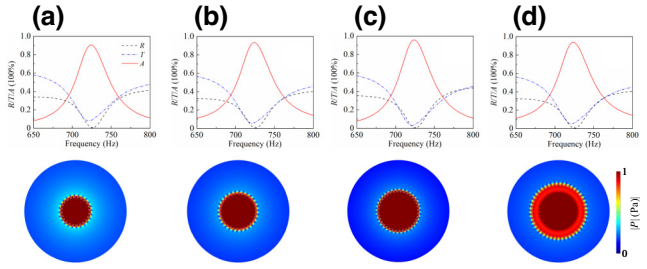


FIG. 13. (a)–(d) Scattering spectra of the AMA with different ring radii under constant ventilation conditions (upper panel). Distributions of the absolute sound pressure in the systems at 724 Hz (lower panel). The radii for these four cases are 0.31, 0.4, 0.47, and 0.61 m, respectively.

ranges from 24 to 45, corresponding to ring radii of 0.31, 0.4, 0.47, and 0.61 m. It is worth mentioning that (1) the operating frequency for all four cases remains at 724 Hz, reaffirming that the resonant frequency is independent of the ring radius and the area ratio of the ventilated channel; and (2) by keeping the filling ratio of the ventilated channel constant, a larger ring radius results in a higher absorptive-peak value. This phenomenon can be attributed to the fact that, as the ring radius increases, the cylindrical wave behaves more like a plane wave, bringing the absorption peak closer to that of the MA.

[1] K. Y. Bliokh, Y. P. Bliokh, V. Freilikher, S. Savel'ev, and F. Nori, Colloquium: Unusual resonators: Plasmonics, metamaterials, and random media, Rev. Mod. Phys. **80**, 1201 (2008).

[2] T. S. Luk, S. Campione, I. Kim, S. Feng, Y. C. Jun, S. Liu, J. B. Wright, I. Brener, P. B. Catrysse, S. Fan, and M. B. Sinclair, Directional perfect absorption using deep subwavelength low-permittivity films, Phys. Rev. B **90**, 085411 (2014).

[3] M. Yang and P. Sheng, Sound absorption structures: From porous media to acoustic metamaterials, Annu. Rev. Mater. Res. **47**, 83 (2017).

[4] J. Li, W. Wang, Y. Xie, B.-I. Popa, and S. A. Cummer, A sound absorbing metasurface with coupled resonators, Appl. Phys. Lett. **109**, 091908 (2016).

[5] V. Romero-García, G. Theocharis, O. Richoux, A. Merkel, V. Tournat, and V. Pagneux, Perfect and broadband acoustic absorption by critically coupled sub-wavelength resonators, Sci. Rep. **6**, 19519 (2016).

[6] V. Achilleos, G. Theocharis, O. Richoux, and V. Pagneux, Non-Hermitian acoustic metamaterials: Role of exceptional points in sound absorption, Phys. Rev. B **95**, 144303 (2017).

[7] N. Jiménez, V. Romero-García, V. Pagneux, and J.-P. Groby, Quasiperfect absorption by subwavelength acoustic panels in transmission using accumulation of resonances due to slow sound, Phys. Rev. B **95**, 014205 (2017).

[8] N. Jiménez, W. Huang, V. Romero-García, V. Pagneux, and J. P. Groby, Ultra-thin metamaterial for perfect and quasi-omnidirectional sound absorption, Appl. Phys. Lett. **109**, 121902 (2016).

[9] H. Long, Y. Cheng, and X. Liu, Reconfigurable sound anomalous absorptions in transparent waveguide with modularized multi-order Helmholtz resonator, Sci. Rep. **8**, 15678 (2018).

[10] D.-Y. Maa, Potential of microperforated panel absorber, J. Acoust. Soc. Am. **104**, 2861 (1998).

[11] V. M. García-Chocano, S. Cabrera, and J. Sánchez-Dehesa, Broadband sound absorption by lattices of microperforated cylindrical shells, Appl. Phys. Lett. **101**, 184101 (2012).

[12] Y. Li, Y. Lin, and Y. Peng, Enhancing sound absorption for an acoustic metastructure with extended tubes at ultra-low frequency, J. Appl. Phys. **132**, 115104 (2022).

[13] C. Zhang and X. Hu, Three-dimensional single-port labyrinthine acoustic metamaterial: Perfect absorption with large bandwidth and tunability, Phys. Rev. Appl. **6**, 064025 (2016).

[14] M. Yang, S. Chen, C. Fu, and P. Sheng, Optimal sound-absorbing structures, Mater. Horiz. **4**, 673 (2017).

[15] H. Long, C. Shao, C. Liu, Y. Cheng, and X. Liu, Broadband near-perfect absorption of low-frequency sound by subwavelength metasurface, Appl. Phys. Lett. **115**, 103503 (2019).

[16] Y. Liu, S. Ren, W. Sun, Y. Lei, H. Wang, and X. Zeng, Broadband low-frequency sound absorbing metastructures based on impedance matching coiled-up cavity, Appl. Phys. Lett. **119**, 101901 (2021).

[17] J. Mei, G. Ma, M. Yang, Z. Yang, W. Wen, and P. Sheng, Dark acoustic metamaterials as super absorbers for low-frequency sound, Nat. Commun. **3**, 756 (2012).

[18] G. Ma, M. Yang, S. Xiao, Z. Yang, and P. Sheng, Acoustic metasurface with hybrid resonances, Nat. Mater. **13**, 873 (2014).

[19] M. Yang, Y. Li, C. Meng, C. Fu, J. Mei, Z. Yang, and P. Sheng, Sound absorption by subwavelength membrane structures: A geometric perspective, C. R. Mec. **343**, 635 (2015).

[20] M. Liu, S. Xia, W. Wan, J. Qin, H. Li, C. Zhao, L. Bi, and C. Qiu, Broadband mid-infrared non-reciprocal absorption using magnetized gradient epsilon-near-zero thin films, Nat. Mater. **22**, 1196 (2023).

[21] H. Long, S. Gao, Y. Cheng, and X. Liu, Multiband quasi-perfect low-frequency sound absorber based on double-channel Mie resonator, Appl. Phys. Lett. **112**, 033507 (2018).

[22] C. Shao, C. Liu, C. Ma, H. Long, K. Chen, Y. Cheng, and X. Liu, Multiband asymmetric sound absorber enabled by ultrasparse Mie resonators, J. Acoust. Soc. Am. **149**, 2072 (2021).

[23] C. Shao, H. Long, Y. Cheng, and X. Liu, Low-frequency perfect sound absorption achieved by a modulus-near-zero metamaterial, Sci. Rep. **9**, 13482 (2019).

[24] X. Peng, J. Ji, and Y. Jing, Composite honeycomb metasurface panel for broadband sound absorption, J. Acoust. Soc. Am. **144**, EL255 (2018).

[25] S. Huang, Z. Zhou, D. Li, T. Liu, X. Wang, J. Zhu, and Y. Li, Compact broadband acoustic sink with coherently coupled weak resonances, Sci. Bull. **65**, 373 (2020).

[26] Z. Zhou, S. Huang, D. Li, J. Zhu, and Y. Li, Broadband impedance modulation via non-local acoustic metamaterials, Natl. Sci. Rev. **9**, nwab171 (2021).

[27] H. Nguyen, Q. Wu, J. Chen, Y. Yu, H. Chen, S. Tracy, and G. Huang, A broadband acoustic panel based on double-layer membrane-type metamaterials, Appl. Phys. Lett. **118**, 184101 (2021).

[28] C. Shao, Y. Zhu, H. Long, C. Liu, Y. Cheng, and X. Liu, Metasurface absorber for ultra-broadband sound via over-damped modes coupling, Appl. Phys. Lett. **120**, 083504 (2022).

[29] J. Xu, X. Zhu, D. Chen, Q. Wei, and D. Wu, Broadband low-frequency acoustic absorber based on metaporous composite, Chin. Phys. B **31**, 064301 (2022).

[30] F. Ma, C. Wang, Y. Du, Z. Zhu, and J. Wu, Enhancing of broadband sound absorption through soft matter, Mater. Horiz. **9**, 653 (2022).

[31] C. Fu, X. Zhang, M. Yang, S. Xiao, and Z. Yang, Hybrid membrane resonators for multiple frequency asymmetric absorption and reflection in large waveguide, Appl. Phys. Lett. **110**, 021901 (2017).

[32] H. Long, Y. Cheng, and X. Liu, Asymmetric absorber with multiband and broadband for low-frequency sound, Appl. Phys. Lett. **111**, 143502 (2017).

[33] N. Jiménez, V. Romero-García, V. Pagneux, and J.-P. Groby, Rainbow-trapping absorbers: Broadband, perfect and asymmetric sound absorption by subwavelength panels for transmission problems, Sci. Rep. **7**, 13595 (2017).

[34] T. Lee, T. Nomura, E. M. Dede, and H. Iizuka, Ultrasparse acoustic absorbers enabling fluid flow and visible-light controls, Phys. Rev. Appl. **11**, 024022 (2019).

[35] K. Donda, Y. Zhu, S. Fan, L. Cao, Y. Li, and B. Assouar, Extreme low-frequency ultrathin acoustic absorbing metasurface, Appl. Phys. Lett. **115**, 173506 (2019).

[36] H. Long, C. Liu, C. Shao, Y. Cheng, J. Tao, X. Qiu, and X. Liu, Tunable and broadband asymmetric sound absorptions with coupling of acoustic bright and dark modes, J. Sound Vib. **479**, 115371 (2020).

[37] X. Xiang, X. Wu, X. Li, P. Wu, H. He, Q. Mu, S. Wang, Y. Huang, and W. Wen, Ultra-open ventilated metamaterial absorbers for sound-silencing applications in environment with free air flows, Extreme Mech. Lett. **39**, 100786 (2020).

[38] V. Romero-García, N. Jiménez, J.-P. Groby, A. Merkel, V. Tournat, G. Theocharis, O. Richoux, and V. Pagneux, Perfect absorption in mirror-symmetric acoustic metascreens, Phys. Rev. Appl. **14**, 054055 (2020).

[39] Y. Zhu, A. Merkel, K. Donda, S. Fan, L. Cao, and B. Assouar, Nonlocal acoustic metasurface for ultrabroadband sound absorption, Phys. Rev. B **103**, 064102 (2021).

[40] C. Liu, J. Shi, W. Zhao, X. Zhou, C. Ma, R. Peng, M. Wang, Z. Hang, X. Liu, J. Christensen, N. X. Fang, and Y. Lai, Three-dimensional soundproof acoustic metacage, Phys. Rev. Lett. **127**, 084301 (2021).

[41] Y. Zhu, H. Long, C. Liu, H. Zhang, Y. Cheng, and X. Liu, An ultra-thin ventilated metasurface with extreme asymmetric absorption, Appl. Phys. Lett. **120**, 141701 (2022).

[42] L. Zhang, W. Zhang, and F. Xin, Broadband low-frequency sound absorption of honeycomb sandwich panels with rough embedded necks, Mech. Syst. Signal Pr. **196**, 110311 (2023).
[43] S. Sergeev, R. Fleury, and H. Lissek, Ultrabroadband sound control with deep-subwavelength plasmacoustic metalayers, Nat. Commun. **14**, 2874 (2023).
[44] S. Elliott and P. Nelson, *Active Control of Sound* (Academic Press, London, 1992).
[45] G. A. Mangiante, Active sound absorption, J. Acoust. Soc. Am. **61**, 1516 (1977).
[46] G. Canevet, Active sound absorption in an air conditioning duct, J. Sound Vib. **58**, 333 (1978).
[47] H. Long, Y. Zhu, Y. Gu, Y. Cheng, and X. Liu, Inverse design of an ultrasparse dissipated-sound metacage by using a genetic algorithm, Phys. Rev. Appl. **18**, 044032 (2022).
[48] M. R. Stinson, The propagation of plane sound waves in narrow and wide circular tubes, and generalization to uniform tubes of arbitrary cross-sectional shape, J. Acoust. Soc. Am. **89**, 550 (1991).
[49] V. Fokin, M. Ambati, C. Sun, and X. Zhang, Method for retrieving effective properties of locally resonant acoustic metamaterials, Phys. Rev. B **76**, 144302 (2007).
[50] ASTM-E2611-09, *Standard Test method for Measurement of Normal Incidence Sound Transmission of Acoustical Materials Based on Transfer Matrix Method* (ASTM International, West Conshohocken, PA, 2009).
[51] J. R. Piper, V. Liu, and S. Fan, Total absorption by degenerate critical coupling, Appl. Phys. Lett. **104**, 251110 (2014).
[52] X. Wu, K. Y. Au-Yeung, X. Li, R. C. Roberts, J. Tian, C. Hu, Y. Huang, S. Wang, Z. Yang, and W. Wen, High-efficiency ventilated metamaterial absorber at low frequency, Appl. Phys. Lett. **112**, 103505 (2018).
[53] I. Dinçer and M. Kanoglu, *Refrigeration Systems and Applications* (John Wiley & Sons, Ltd, West Sussex, 2010), 2nd ed.